

# Observation and modelling of ion cyclotron range of frequencies waves in the mode conversion region of Alcator C-Mod

Y Lin<sup>1</sup>, S Wukitch<sup>1</sup>, A Parisot<sup>1</sup>, J C Wright<sup>1</sup>, N Basse, P Bonoli<sup>1</sup>,  
E Edlund<sup>1</sup>, L Lin<sup>1</sup>, M Porkolab<sup>1</sup>, G Schilling<sup>2</sup> and P Phillips<sup>3</sup>

<sup>1</sup> Massachusetts Institute of Technology, Plasma Science and Fusion Center, Cambridge, MA 02139, USA

<sup>2</sup> Princeton Plasma Physics Laboratory, Princeton, NJ 08543, USA

<sup>3</sup> Fusion Research Center, University of Texas, Austin, TX 78712, USA

E-mail: [ylin@psfc.mit.edu](mailto:ylin@psfc.mit.edu)

Received 17 February 2005, in final form 31 March 2005

Published 19 July 2005

Online at [stacks.iop.org/PPCF/47/1207](http://stacks.iop.org/PPCF/47/1207)

## Abstract

The fast magnetosonic wave, mode converted ion cyclotron wave (MC ICW) and mode converted ion Bernstein wave (MC IBW) have all been observed and unambiguously identified in the mode conversion region of Alcator C-Mod. The influences of the species mix, mode conversion location and  $B_{\text{pol}}/B_{\text{tot}}$  have been studied in D(<sup>3</sup>He) plasmas at  $B_0 \sim 5.4$  T ( $f_{\text{RF}} = 50$  MHz) and  $B_0 \sim 8$  T ( $f_{\text{RF}} = 78$  MHz). The RF waves were measured by a phase contrast imaging (PCI) system. The experimental observation is compared with the result from a synthetic PCI diagnostic based upon the full wave code TORIC. Good agreement between the observation and modelling has been obtained on the spatial structure of the RF waves. When the mode conversion layer was off axis, both MC ICW and MC IBW were observed. In 5.4 T near-axis mode conversion discharges, the double hump spatial structure of the MC waves was observed experimentally and reproduced by the synthetic PCI. Such a structure is an indication of the up–down asymmetry of the MC ICW. In 8 T near-axis mode conversion discharges, we had the first definitive observation of IBW dominated MC in Alcator C-Mod.

(Some figures in this article are in colour only in the electronic version)

## 1. Introduction

Ion cyclotron range of frequencies (ICRF) radio wave heating is one of the major auxiliary heating methods in magnetically confined fusion research. An ICRF heated plasma is usually a multi-species plasma, for example, a D(<sup>3</sup>He) plasma, with <sup>3</sup>He as the minority species and deuterium as the majority species. At low <sup>3</sup>He concentration ( $n_{\text{He}}/n_e \leq 0.05$ ), the fast magnetosonic wave (fast wave, or FW), launched by the antenna is mostly absorbed by the <sup>3</sup>He ions

at the  $^3\text{He}$  cyclotron resonance layer [1]. When the  $^3\text{He}$  level is moderate ( $n_{^3\text{He}}/n_e \geq 0.1$ ), the FW is partially mode converted to short wavelength waves near the D- $^3\text{He}$  hybrid layer [2–6]. The mode converted waves may be used to directly heat electrons (e.g., see [7–11]), drive current [12, 13] and potentially plasma flow [4, 14], etc. In this paper, we report the first comprehensive study on the experimental observation and numerical modelling of ICRF waves, including the FW and short wavelength waves, in the mode conversion region of the Alcator C-Mod tokamak.

The ion–ion hybrid layer (MC layer) is defined in the cold plasma limit as  $n_{\parallel}^2 = S$ , where  $n_{\parallel}$  is the FW refractive index parallel to the  $B$  field.  $S = 1 - \sum_{j=i,e} \omega_{pj}^2 / (\omega^2 - \omega_{cj}^2)$  in the cold plasma approximation, where  $j$  denotes particle species,  $\omega_{pj}$  is the plasma frequency,  $\omega_{cj}$  is the ion (electron) cyclotron frequency and  $\omega$  is the launched RF wave frequency [15]. On the high-field side (HFS) of the MC layer, the FW can be mode converted to an ion Bernstein wave (IBW), which propagates to the HFS. The MC IBW is a warm plasma slow wave, which only exists with finite ion temperature, with wavelength in the order of  $k_{\perp} \rho_i \sim 1$ , where  $\rho_i$  is the Larmor radius and  $k_{\perp}$  is the wave number perpendicular to the magnetic field. It is also a backward wave, i.e. its phase velocity is towards the low-field side (LFS). On the LFS of the MC layer, the FW can be converted to the MC ion cyclotron wave (ICW), propagating to the LFS. The ICW is a short wavelength wave originating from the magnetic field line rotational transformation in a toroidal plasma confinement device. While the toroidal mode number  $n_{\phi}$  of the FW is fixed by the toroidal symmetry,  $n_{\parallel}$  can be up-shifted to such a level that a short wavelength mode admissible by the local dispersion relation exists in the vicinity of the LFS side of the MC layer [2]. Depending on plasma conditions, such as  $B$  field, species concentration, plasma current, density and temperature profile, the relative levels of the FW, MC IBW and MC ICW can vary significantly. In cases where the ratio of poloidal  $B$  field strength to total  $B$  field strength  $B_{\text{pol}}/B_{\text{tot}} \ll 1$  near the MC layer, the MC IBW can be the only MC wave. In a previous experimental study, the MC ICW was observed using a PCI system in D(H,  $^3\text{He}$ ) plasmas near the H- $^3\text{He}$  hybrid layer in Alcator C-Mod [3]. In the experiments reported in [3], the PCI view was on the LFS of the MC layer. The observed wave was identified as the MC ICW by comparing the observations with the simulations using a full wave toroidal ion cyclotron (IC) wave code TORIC [16, 17]. Further studies have been performed on mode conversion electron heating (MCEH) and power partition between the MC ICW and IBW [5, 7]. Recent comparison of PCI measurements and TORIC have shown that the TORIC physics kernel and the computational algorithm describe the MC physics well [13, 18]. In the study presented in this paper, the FW, MC ICW and MC IBW have all been observed, sometimes simultaneously, using an upgraded PCI system in D( $^3\text{He}$ ) plasmas. A significantly enhanced TORIC code has also made feasible, a more realistic comparison between experiments and simulations (see section 2.3 and [6]). Using the upgraded PCI and TORIC, we have studied the influences on the mode conversion of the species mix, MC layer location and  $B_{\text{pol}}/B_{\text{tot}}$ .

This paper is organized as follows. Section 2 describes the experimental set-up, the PCI diagnostic and the synthetic PCI based upon TORIC. In section 3, the experimental PCI results are compared with the synthetic PCI results. Off-axis mode conversion and near-axis mode conversion are presented separately in sections 3.1 and 3.2, followed by discussion and future work in section 4 and section 5 gives a summary.

## 2. Setup of experiments and simulations

### 2.1. Experimental set-up

Alcator C-Mod is a compact ( $R \simeq 0.67$  m,  $a \simeq 0.22$  m), high field ( $B \leq 8.1$  T) tokamak [19]. For experiments reported here, the RF power was provided by a phase-variable 4-strap antenna

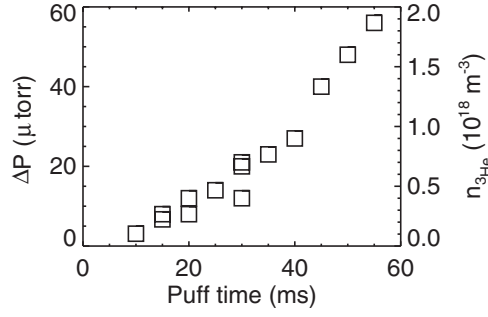


**Figure 1.** Gas pressure rise versus  $^3\text{He}$  puffing. The left scale is the measured pressure, whereas the right scale is the equivalent  $^3\text{He}$  atom density. Data was collected during beam-into-gas calibration for the motional Stark effect (MSE) diagnostic.

in J-port (J-antenna) [20]. The RF power level was  $P_{\text{RF}} \leq 3$  MW. The RF frequency was at 50 MHz for experiments of  $B \sim 5.2$ – $5.6$  T and at 78 MHz for experiments of  $B \sim 7.7$ – $8.1$  T. The four antenna straps were configured to  $[0, \pi, \pi, 0]$  phasing, which gave the peak toroidal mode number of the launched FW  $n_\phi \simeq \pm 6$  and  $\pm 7$ . The plasmas were in the low confinement mode (L-mode), comprised of D (majority),  $^3\text{He}$  (minority) and residual H. The ratio  $n_{\text{H}}/n_{\text{D}}$  was calculated from the spectroscopic measurement of  $\text{D}_\alpha$  and  $\text{H}_\alpha$  lines at the plasma edge [21]. A flat H/D ratio profile is assumed.  $^3\text{He}$  was introduced by gas puff in the early stage of the plasma discharge. No diagnostic was available to measure the absolute  $^3\text{He}$  level. The amount of  $^3\text{He}$  gas puffed into the vessel is roughly linear as a function of the puffing time (figure 1). The  $^3\text{He}$  level in the plasma is estimated from the MCEH profile, which is calculated from the break-in-slope analysis of  $T_e$  signals measured by a high spatial and temporal resolution electron cyclotron emission (ECE) system [22]. The power deposition profile is calculated using the following equation,

$$S_{\text{exp}}^{\text{mc}} \simeq \frac{3}{2} n_e \left| \Delta \frac{dT_e}{dt} \right|, \quad (1)$$

where  $\Delta dT_e/dt$  is the change of the slope of  $T_e$  signal before and after an RF shut-off. Since the mode conversion region is narrow, the  $^3\text{He}$  level can be rather accurately estimated by matching the MCEH profile from TORIC with the one from break-in-slope analysis (see section 3.1).

## 2.2. PCI system and data analysis

The PCI system in Alcator C-Mod measures the line-integrated density fluctuations [23–25]. The PCI laser is located at the E-port and toroidally  $216^\circ$  away from the J-antenna (figure 2(a)). The system presently has 32 channels (vertical chords) covering a window from major radius  $R = 0.64$  to  $0.76$  m (figure 2(b)). The separation between channels is  $\Delta R \simeq 0.4$  cm. As a result, the PCI system can measure wave numbers  $k_R$  in the range of  $\pm(0.5$ – $8)$   $\text{cm}^{-1}$  without spatial aliasing. The upper limit of PCI sensitivity is  $k_{\text{lim}} \simeq 17$   $\text{cm}^{-1}$ , determined by the element size of the detectors and optical expansion. To measure waves at the RF frequency, the PCI laser is modulated in intensity at a frequency near the RF frequency of interest. The modulation is done by splitting the beam, upshifting the one half and downshifting the other using acoustic-optical modulators (AOMs), then recombining the two halves before entering the plasma. The ICRF waves appear in the PCI signal at the beat frequency between the RF frequency and the modulation frequency. The PCI system is most sensitive to waves having vertical wave fronts and propagating in the direction of major radius. Because no vertical resolution is

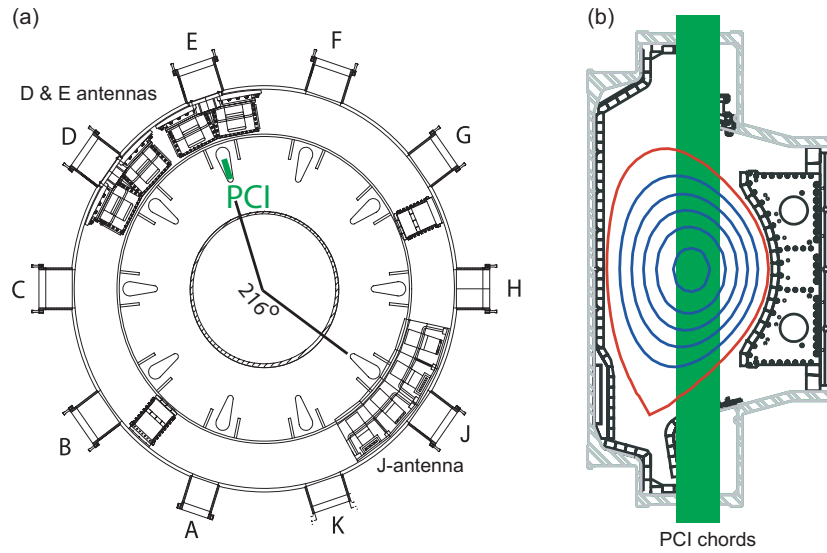


**Figure 2.** (a) The toroidal view of Alcator C-Mod, (b) PCI layout.

available in the present PCI system, the resulting measurement is a superposition of waves along vertical lines.

The PCI signal in each channel is sampled at 10 MHz for about 0.5 s. Each signal is divided into 10 ms time windows, and the data in each time window are Fourier transformed to the complex spectrum of  $A \exp(-i\omega t + i\theta)$ . Figure 3 shows an example of the Fourier transformed PCI signal. The coherent peak at  $f = \omega_{\text{beat}}/2\pi = 970.4$  kHz in this figure is the magnitude of the density fluctuations directly induced by the RF waves. By doing the same analysis on all 32 channels, we can show the spatial structure of the RF waves by the real and imaginary parts of the complex spectrum at this beat frequency versus PCI channel locations. From the phase difference  $\Delta\theta$  between channels at this beat frequency, we can also calculate a local wave number,  $k_{\text{loc}} = \Delta\theta/\Delta R$ .  $k_{\text{loc}}$  can approximately represent the dispersion curve of the dominant wave in the PCI view in cases where the wave has nearly vertical wave fronts. Doing Fourier transformation of the complex signal again over all 32 channels, we can calculate the  $k_R$  spectrum of the PCI measurement. Caution must be taken, however, in interpreting this  $k_R$  spectrum because mode conversion is substantially localized and a rapid change of wave number often occurs in a narrow region.

The PCI system is calibrated 1 s before each discharge using a sound burst across the laser beam, before the laser beam enters the vacuum window [23]. This calibration provides the information of the width in major radius covered by the PCI view, and also the fluctuation level corresponding to the sound wave. However, it appears inadequate using the sound burst (spherical wave approximation) calibration data to obtain the density fluctuations for the heterodyne measurement. Using the calibration data above produces density fluctuation levels that are systematically about two orders of magnitude smaller than those estimated from the RF power. There are a couple of issues of the PCI diagnostics that are not taken into account in this calibration. For example, the responses of the pre-amplifiers at the heterodyne beat frequencies (970 kHz for  $f_{\text{RF}} = 50$  MHz and 1740 kHz for  $f_{\text{RF}} = 78$  MHz) can be a factor of  $\leq 2$  lower than that at the sound wave (15 kHz). The conversion efficiencies of the AOMs are not known precisely, which can introduce a factor of  $\leq 2$  also. Moreover, a drift

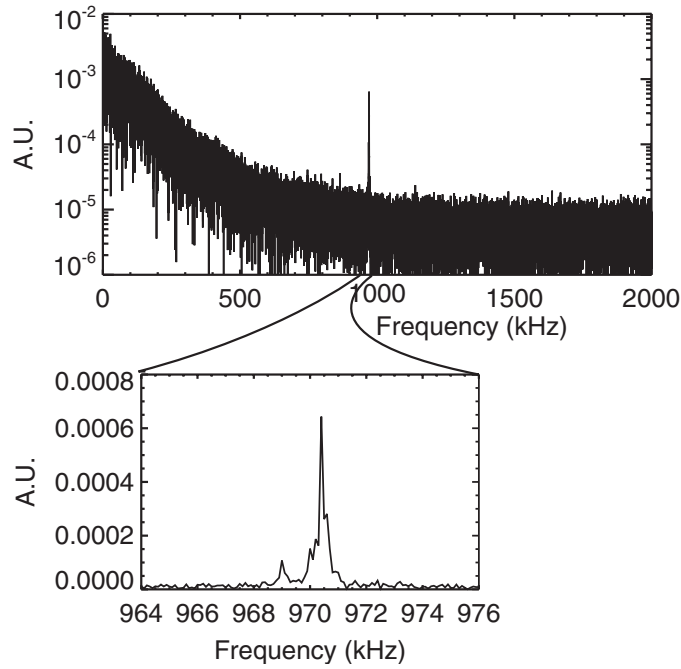


**Figure 3.** An example of the Fourier transformed PCI signal. The frequency at the coherent peak, 970.4 kHz, is the beat frequency corresponding to the RF frequency at 50 MHz. The small peak at 969 kHz is a pick-up spurious signal from the detector circuitry.

in the alignment of the two split beams can also affect the level of the heterodyne signal. Considering all these issues, the absolute level obtained from this sound burst calibration may underestimate the density fluctuation by a factor of  $\leq 20$ . Other possible factors are still under investigation. In this paper, the PCI results are multiplied by a correction factor of 300 for the 50 MHz experiments, and a factor of 100 for the 78 MHz experiments. The different correction factors may be owing to the difference in laser alignment on different experimental days. After this correction, the experimental result in terms of line-integrated density level is comparable to that from a synthetic PCI (see below). The absolute level calibration for the heterodyne scheme will be the subject of future work.

### 2.3. TORIC and synthetic PCI

TORIC is a two-dimensional finite Larmor radius (FLR) full wave RF code [16, 17], which solves Maxwell's equations in a toroidal plasma at a fixed RF frequency and a given toroidal number  $n_\phi$ . The electric field is solved in a mixed spectral and finite-element basis. To properly calculate the electron Landau damping (ELD) of the short wavelength modes (IBW/ICW), an imaginary part is added on the FLR coefficient [6, 10]. This imaginary part is calculated from the local dispersion relation retaining all orders of  $k_\perp \rho_i$ . This approach calculates the ELD predicted by the local dispersion relation without altering the structure of the equations, or changing the mode conversion efficiency. Additionally, this approach lends itself to efficient numerical calculation resulting from the sparse, block tridiagonal nature of its stiffness matrix. Incorporating the magnetic equilibrium from EFIT [26], instead of an analytic model equilibrium (including the paramagnetic effect on  $B_{\text{tor}}$ , which had been

previously neglected) into the parallel TORIC code improves the simulation to reproduce more closely the experimental measurement, even in the small spatial scale relevant to the mode conversion process. The parallel version of the code, ran on a 48-CPU cluster at the MIT Plasma Science and Fusion Center, is also able to do larger resolutions needed to converge mode conversion cases and can be run for the entire antenna spectrum for many discharges in a reasonable time, thus permitting a thorough and accurate survey of the experimental cases. TORIC has been benchmarked with other ICRF codes. It is found to have good agreement with METS [27] in the power absorption on electrons and ions [10]. A qualitative agreement with AORSA2D [4] in the two-dimensional electric fields in mode conversion scenarios, where  $k_{\perp}\rho_i \leq 1$  [6] has also been obtained. The code has been extensively benchmarked with ICRF mode conversion experiments in Alcator C-Mod (e.g. see [5, 7, 13, 18]).

In order to compare the PCI measured density fluctuations at the beat frequency and the RF wave field in the plasma, we have developed a synthetic PCI using TORIC outputs. TORIC calculates the electric field, power deposition profile (such as the mode conversion power deposition profile  $S_{\text{toric}}^{\text{mc}}(n_{\phi}, \rho)$ , where  $\rho = r/a$ ) and the coupling resistance  $R_L(n_{\phi})$  for a 1 A excitation on the antenna straps. For each plasma discharge of interest, TORIC simulations for toroidal numbers  $-20 \leq n_{\phi} \leq +20$  are performed. The antenna spectrum beyond  $-20 \leq n_{\phi} \leq +20$  is negligible. The two-dimensional density fluctuation  $n_{e1}(n_{\phi})$  is calculated from the electric field for each  $n_{\phi}$  using the fluid approximation ( $\omega \ll \omega_{pe} \sim \omega_{ce}$ ) [28]. Approximately, the result can be expressed in the following equations (SI units)

$$n_{e1} \approx -\frac{i}{\omega} n_{e0} \nabla \cdot \vec{v}_{e1}, \quad (2)$$

where

$$v_{e1,\parallel} \approx -\frac{i\omega_{ce}}{\omega} \frac{E_{\parallel}}{B} \quad (3)$$

and

$$v_{e1,\perp} \approx \frac{E_{\perp}}{B}. \quad (4)$$

The subscript ‘1’ on electric fields has been dropped for clarity. For the FW, which has a negligible  $E_{\parallel}$ , the component of the electric field parallel to  $B$  field, its contribution to  $n_{e1}$  is mainly from the perpendicular field  $E_{\perp}$ . For the MC waves,  $E_{\parallel}$  is about two orders of magnitude smaller than  $E_{\perp}$ , but the contribution from  $E_{\parallel}$  is often comparable or larger because of the factor  $\omega_{ce}/\omega \sim m_i/m_e$ . The density fluctuation that can be compared with experimental measurement is the sum of  $n_{e1}(n_{\phi})$  weighted by  $R_L(n_{\phi})$  and the antenna current spectrum  $j(n_{\phi})$ , where  $\sum |j(n_{\phi})|^2 = 1$ , and also total input RF power  $P_{\text{RF}}$ ,

$$n_{e1} = \sum_{n_{\phi}=-20}^{20} n_{e1}(n_{\phi}) j(n_{\phi}) e^{in_{\phi}\Delta\phi} \sqrt{\frac{P_{\text{RF}}}{R_L^{\text{tot}}}}, \quad (5)$$

where  $\Delta\phi = 216^\circ$  is the toroidal angle from the centre of J-antenna to the PCI chords, and the total coupling resistance

$$R_L^{\text{tot}} = \sum_{n_{\phi}=-20}^{20} |j(n_{\phi})|^2 R_L(n_{\phi}). \quad (6)$$

The PCI measurement is modelled as the line integral of this two-dimensional  $n_{e1}$  along 32 vertical chords. The finite detector element size imaged into the plasma is modelled as a simple average over a width of about 0.4 cm. Equation (6) is also used to obtain the

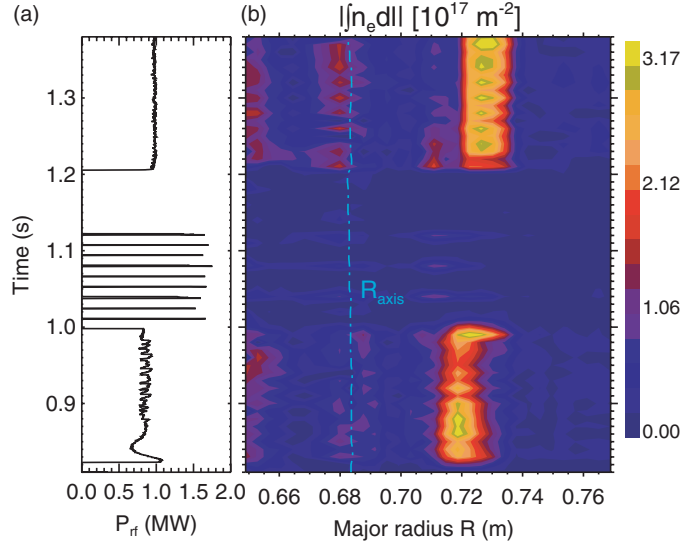


**Figure 4.** A discharge with off-axis mode conversion.  $f_{\text{RF}} = 50$  MHz,  $B_{\text{axis}} = 5.57$  T,  $n_{\text{H}}/n_{\text{e}} = 3\%$ ,  $n_{\text{D}}/n_{\text{e}} = 75\%$ ,  $n_{\text{3He}}/n_{\text{e}} = 11\text{--}12\%$ . (a) RF power versus time, (b) the PCI measured line-integrated fluctuation level at the beat frequency versus time and major radius.

power deposition profile from TORIC. For example, the power deposition profile from mode conversion is calculated as

$$S_{\text{toric}}^{\text{mc}}(\rho) = \sum_{n_{\phi}=-20}^{20} |j(n_{\phi})|^2 S_{\text{toric}}^{\text{mc}}(n_{\phi}, \rho) \frac{P_{\text{RF}}}{R_{\text{L}}^{\text{tot}}}, \quad (7)$$

which can be compared with the experimental result from equation (1).

### 3. Results

Using the experimental PCI and synthetic PCI, we have studied the influences on the mode conversion of the species mix, MC layer location and  $B_{\text{pol}}/B_{\text{tot}}$ . The results are presented in the following two sections—off axis and near axis—based on the MC layer location relative to the magnetic axis. In each section, discharges at two different  $B$  fields and RF frequencies are also compared.

#### 3.1. Off-axis mode conversion

In figure 4, we show the PCI data of a discharge, where the mode conversion is off axis on the LFS. In this figure, the PCI line integrated fluctuations caused by the RF waves are plotted versus major radius and time. The input RF power is also plotted. The plasma parameters are  $I_{\text{p}} = 1.0$  MA,  $n_{\text{e}0} = 2.0 \times 10^{20} \text{ m}^{-3}$ ,  $T_{\text{e}0} = 2.1$  keV and  $T_{\text{i}} \simeq T_{\text{e}}$ ,  $n_{\text{H}}/n_{\text{D}} = 4\%$ ,  $R_{\text{axis}} = 0.683$  m and  $B_{\text{axis}} = 5.57$  T. The RF frequency  $f_{\text{RF}} = 50$  MHz.  $^3\text{He}$  gas is puffed for 150 ms from  $t = 0.3$  to  $t = 0.45$  s. A peak is clearly shown in the PCI signal around  $R = 0.72\text{--}0.73$  m when the RF is on. The peak moves to the LFS by about 1 cm in time. This can be explained by the slow depletion of  $^3\text{He}$  ions in the plasma during the discharge. In figure 5, we plot the power deposition profiles from TORIC simulations at different  $^3\text{He}$  levels

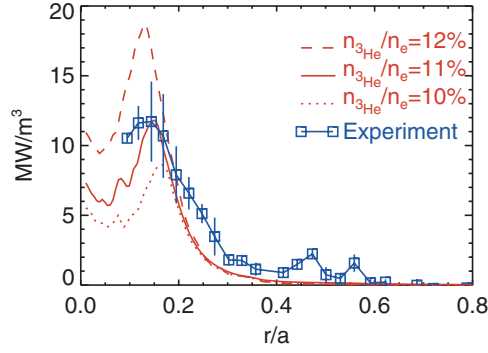


**Figure 5.** Comparison of the mode conversion direct electron heating profiles. The experimental curve is calculated from the break-in-slope of  $T_e$  signals at a fast RF shut-off at  $t = 1.08$  s.

and also compare with the experimental curve, which is calculated from the break in slope in  $T_e$  signals at the RF shut-off at  $t = 1.08$  s. The TORIC curve of  $n_{^3\text{He}}/n_e = 11\%$  matches the experimental curve the best, whereas the other two TORIC curves differ either in the level or location. The possibility that the MC layer is on the HFS of the axis is excluded by comparing discharges in a  $B$  field scan while other parameters are fixed. From the curve of  $n_{^3\text{He}}/n_e = 11\%$ , TORIC predicts that 37% incident power is absorbed directly by electrons through mode conversion. A variation in electron density by 10%, approximately the error bar in density measurement, would vary the mode conversion efficiency in the range of 36–42%. The experimental result is  $38 \pm 8\%$ , obtained by volume integration ( $r/a \leq 0.4$ ) of the experimental curve in figure 5. Therefore, we can constrain the uncertainty of the  $^3\text{He}$  level to be within  $\pm 1\%$  by matching the power deposition profiles. On the other hand, such a constraint also determines the location of the MC layer on the mid-plane to be within  $\pm 0.5$  cm. Considering the variation of the peak location in figure 4, a value of 12% may be better for the earlier part of the discharge and 10% for the later part of the discharge.

In figure 6, we show the two-dimensional contours of the parallel electric field  $E_{\parallel}$  from the TORIC simulation of  $n_{\phi} = 7$  for the above discharge at  $t = 1.38$  s. The MC layer ( $\text{D}^{-3}\text{He}$  hybrid layer), D and  $^3\text{He}$  IC resonance layers are also plotted. The field is plotted in logarithmic scale so that all ICRF waves are shown. There are two different short wavelength structures on the HFS and LFS of the MC layer, respectively. On the HFS, it is the MC IBW and on the LFS, it is the MC ICW. In figure 7, the two-dimensional contours of the density fluctuations caused by the RF wave are plotted (also in logarithmic scale), which shows that the MC waves are the major contributors to the density fluctuations, whereas the FW contribution is insignificant. We then do line integration of  $n_{e1}$  along the vertical PCI chords, do summation using equation (5) and compare the result with the experimental PCI (figure 8). Excellent agreement between experimental data and synthetic output is shown in the structure of both real and imaginary parts of the line integrated density fluctuations. Spatially damped wave structures with wavelength in the order of 1 cm are present on both sides of the MC layer. In figure 8(c), a full width at half maximum (FWHM) of about 2 cm is shown in the fluctuation level. We also compare the  $k_R$  spectra in figure 9. Both experimental PCI and synthetic PCI show a broad peak at  $k_R = 3\text{--}6\text{ cm}^{-1}$ . A positive  $k_R$  indicates that the wave phase velocity is towards the LFS. Such a  $k_R$  spectrum is expected from the two-dimensional plot in figure 7, which shows similar wavelengths for the IBW and ICW near the MC layer. To further show the local wave structure, we plot  $k_{\text{loc}}$  calculated from the phase information between PCI

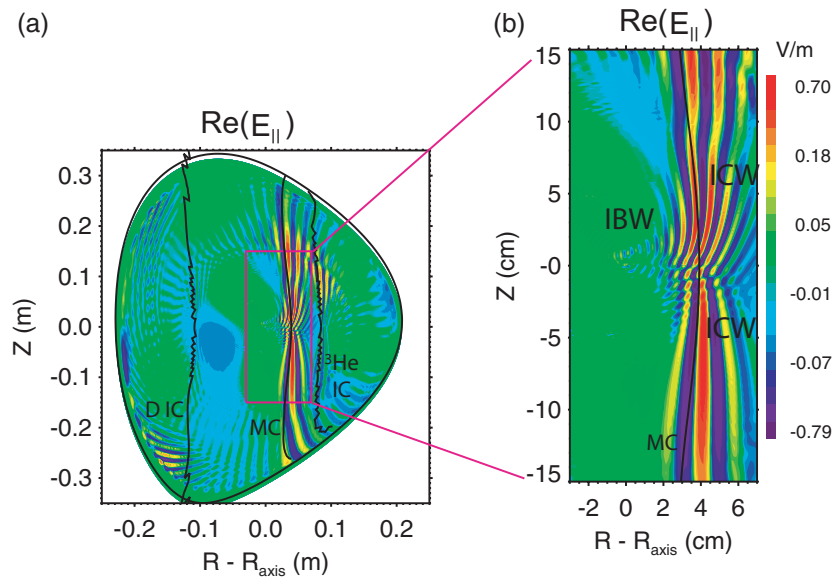


**Figure 6.**  $E_{\parallel}$  field from TORIC simulation ( $n_{\phi} = +7$  and 1 A antenna current) at  $t = 1.38$  s of the discharge in figure 4. The MC layer,  $^3\text{He}$  and D resonance layers are also plotted.

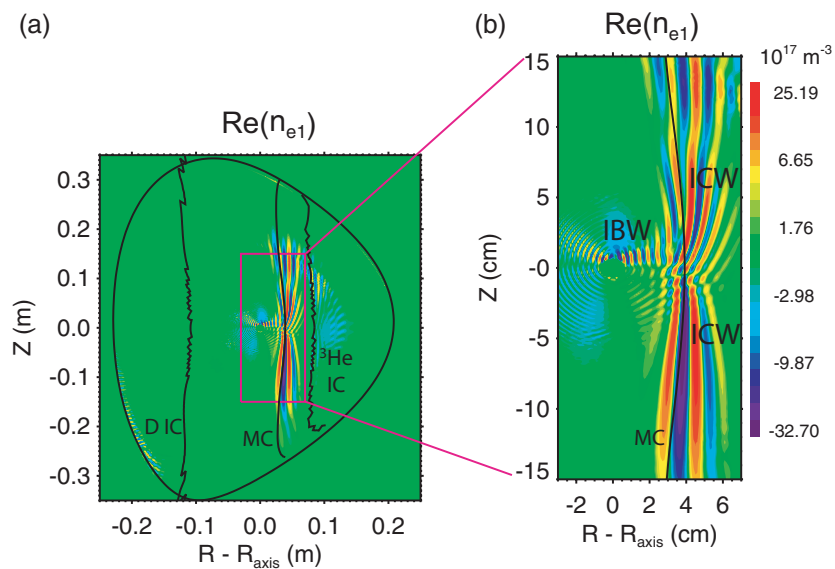


**Figure 7.** Two-dimensional density fluctuations calculated by the synthetic PCI ( $n_{\phi} = +7$ ).

channels in figure 10(a) and compare it with the dispersion curves in figure 10(b). In the region where the PCI signals are large,  $k_{\text{loc}}$  is close to  $4\text{--}5 \text{ cm}^{-1}$  for both experimental PCI and synthetic PCI, in agreement with the spectrum shown in figure 9. In contrast to the dispersion curves in figure 10(b), there is no sudden change in  $k_{\text{loc}}$  in the MC region in both experimental and synthetic  $k_{\text{loc}}$  curves. Neither is there a rapid increase of the IBW wavenumber toward

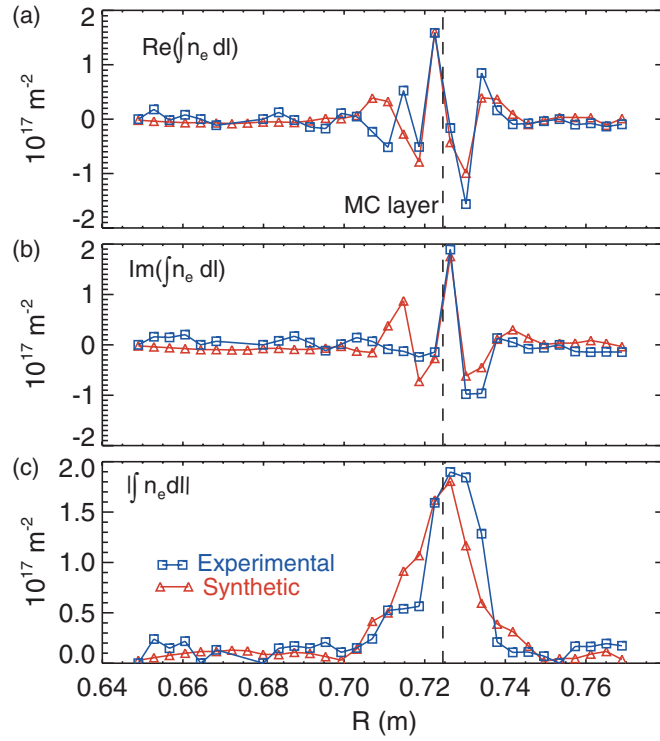


**Figure 8.** Experimental and synthetic PCI line integrated density fluctuations for the discharge in figure 4: (a) real part, (b) imaginary part, (c) magnitude.

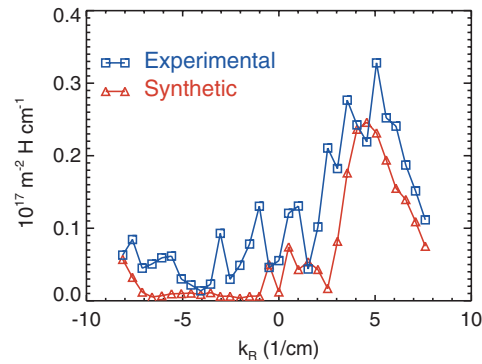


**Figure 9.**  $k_R$  spectra of the experimental and synthetic PCI line integrated density fluctuations of the discharge in figure 4.

the HFS. Instead, figure 10(a) shows that about 1–2 cm away from the MC layer,  $k_{loc}$  decreases rapidly. This apparent discrepancy can be explained by the line integration nature of the PCI measurement and also the two-dimensional structure of the MC waves. First, the MC layer is not a vertical line (see figures 6 and 7), and it is more curved near the mid-plane due to finite  $\beta_p$ , the ratio of plasma pressure and poloidal magnetic field pressure. Moreover, the MC locations are slightly different for different  $n_\phi$ . Second, in locations away from the MC layer,

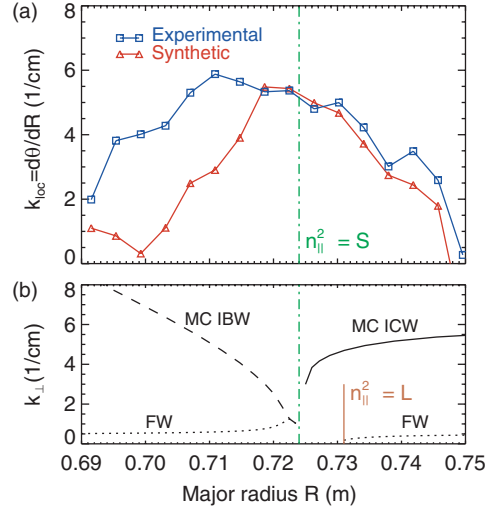


**Figure 10.** (a) Local wave number  $k_{loc} = d\theta/dR$  from experimental measurements and synthetic PCI, (b) dispersion curves. IBW and FW are calculated from the mid-plane, whereas the ICW is calculated along the magnetic surface. The MC layer  $n_{||}^2 = S$  and the left-cutoff layer  $n_{||}^2 = L$  is also plotted.  $L$  is the usual Stix' notation [15].

the FW level becomes comparable or even greater than either the MC ICW or MC IBW, which are more heavily damped. As shown in figures 8(a) and (b), about 2 cm away from the MC layers, the long wavelength FW gradually dominates the PCI measurements.  $k_{loc}$  is sensitive to this ratio of FW and MC waves. The difference in the two  $k_{loc}$  curves on the HFS of the MC layer shown in figure 10(a) is owing to a small difference in the ratios of FW and IBW in the experimental PCI and synthetic PCI. In all, the PCI observation can rarely reproduce the local structure in the dispersion curves shown in figure 10(b), which may only be possible using a diagnostic with sufficient spatial localization capability and  $k$ -space filtering.

The experimental PCI observations of off-axis mode conversion in  $B \sim 8$  T and  $f_{RF} = 78$  MHz are similar. In figure 11, we show the PCI data in such a discharge. The plasma parameters are  $B_{axis} = 7.81$  T,  $I_p = 1.2$  MA,  $n_{e0} = 2.1 \times 10^{20} \text{ m}^{-3}$ ,  $T_{e0} = 4.1$  keV and  $T_i \simeq T_e$ ,  $n_H/n_D = 5\%$ . The  $^3\text{He}$  puff time is the same as the discharge in figure 4. We use  $n_{^3\text{He}}/n_e \simeq 12\%$  for TORIC simulations. In figure 12, the experimental PCI and synthetic PCI are compared. Good agreement is also shown in the real part, imaginary part and magnitude of the fluctuations. Similar to figure 8, short wavelength wave structures exist on both sides of the MC layer. Figure 13 shows the  $k_R$  spectra of the experimental PCI and the synthetic PCI. The MC waves are shown as a broad peak at  $k_R \sim 3\text{--}5 \text{ cm}^{-1}$  in both spectra similar to that in figure 9.

The two-dimensional structure of the MC waves is different. In figure 14 we show the contour of the density fluctuations from the synthetic PCI ( $n_\phi = 7$ ). Unlike in figure 7, the MC ICWs in both upper and lower planes start to propagate significantly farther away from the mid-plane. The wave number of a wave can undergo transformation along the wave path following the approximate equation,

$$k_{||} \approx \frac{n_\phi}{R} \frac{B_\phi}{B_{tot}} + \frac{m}{r} \frac{B_{pol}}{B_{tot}}, \quad (8)$$

where  $m$  is the poloidal mode number.  $m$  is not conserved along the wave path. The ICW only exists where the up-shift of  $k_{||}$  in equation (8) is significant. This condition cannot be fulfilled when  $B_{pol}/B_{tot} \ll 1$ , e.g. near the magnetic axis. Because the distance from the MC layer

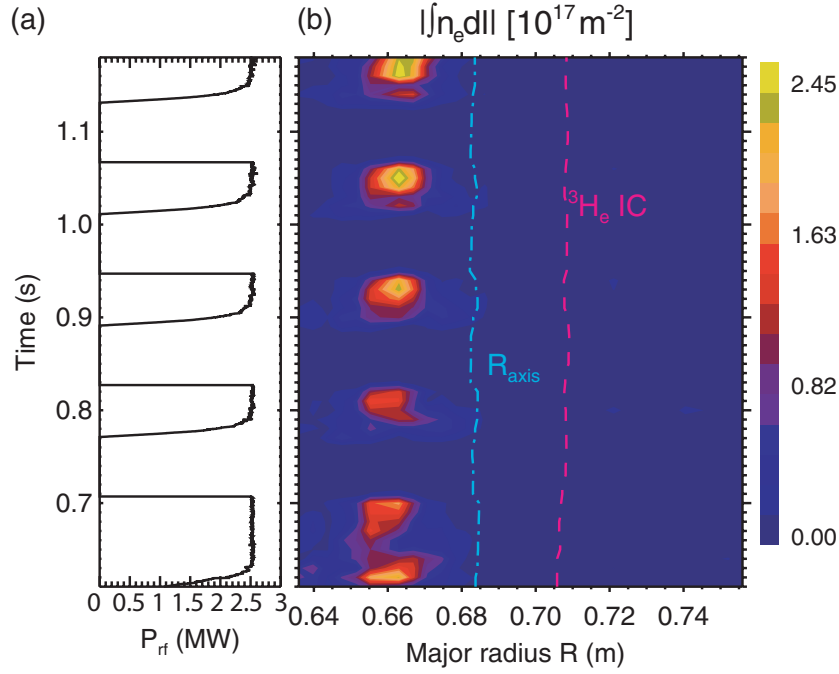


**Figure 11.** A discharge with off-axis mode conversion.  $f_{RF} = 78$  MHz,  $B_{axis} = 7.81$  T,  $n_H/n_e = 5\%$ ,  $n_D/n_e = 72\%$ ,  $n_{^{13}\text{He}}/n_e = 12\%$ . (a) RF power versus time, (b) the PCI measured line-integrated fluctuation level versus time and major radius.

to the magnetic axis in this discharge ( $\approx 2.5$  cm) is smaller than that of figure 4 ( $\approx 4.3$  cm),  $B_{pol}/B_{tot} \approx 0.04$  at the MC layer on the mid-plane of this discharge is only about half of the value,  $B_{pol}/B_{tot} \approx 0.08$ , in the discharge of figure 4. (Note that this discharge not only has a higher  $B$  field but also a higher current.) As a result, the mode conversion to the ICW occurs in locations farther away from the mid-plane. It is worth pointing out that the MC ICW above the mid-plane appears at  $Z \geq 10$  cm, whereas the ICW below the mid-plane appears at about  $Z \approx -4$  cm for this  $n_\phi = +7$ . Such asymmetry can also be explained by equation (8). Note for a wave propagating toward the LFS, it has  $m < 0$  above the mid-plane and  $m > 0$  below the mid-plane. To have a large  $|k_{||}|$ , a larger second term in equation (8) is required for  $m < 0$  than for  $m > 0$ . Such a requirement makes the mode conversion to ICW more favourable below (above) the mid-plane for  $n_\phi > 0$  ( $n_\phi < 0$ ).

In summary, when the MC layer was off axis, the PCI diagnostic observed spatially damped short wavelength waves on both sides of the MC layer. The experimental result is in good agreement with the synthetic PCI result. The two MC waves are clearly distinguishable as the MC IBW and MC ICW in TORIC simulations.

### 3.2. Near-axis mode conversion

In figure 15, we show a discharge with the same parameters as that in figure 4, except a lower  $B$  field ( $B_{axis} = 5.41$  T). The structure of the MC waves in PCI moves toward a smaller major radius, accordingly. Interestingly, the broad single peak in figure 4 is split into two distinct peaks. The dip between these two peaks also evolves during the discharge. This double hump structure in PCI measurements appears in several discharges where the MC layer is near

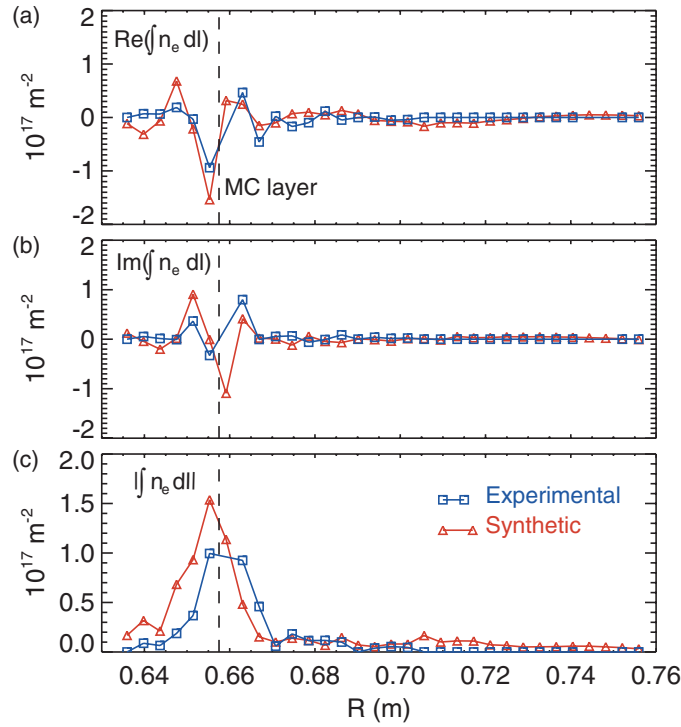


**Figure 12.** Experimental and synthetic PCI line integrated density fluctuations for the discharge in figure 11: (a) real part, (b) imaginary part, (c) magnitude.

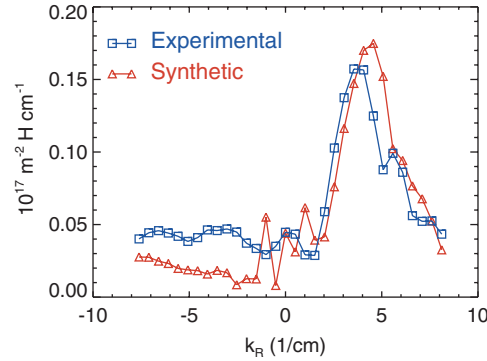


**Figure 13.**  $k_R$  spectra of the experimental and synthetic PCI line integrated density fluctuations of the discharge in figure 11.

the axis. The dip can appear in different channels, which rules out the possibility of a bad PCI channel. In figure 16, we compare the experimental result with the synthetic PCI output ( $n_{3\text{He}}/n_e = 12\%$ ). The real and imaginary part of the density fluctuations both show short wavelength waves on both sides of the MC layer. The synthetic PCI also has a double hump structure as seen in figure 16(c), which shows the magnitude of the fluctuations. The dip of the double hump structure is close to the MC layer.

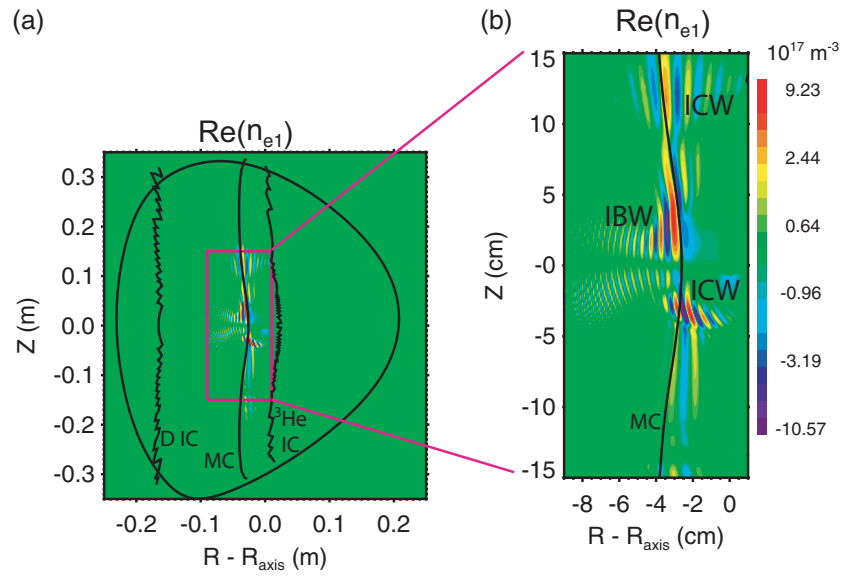


**Figure 14.** Two-dimensional density fluctuations calculated by the synthetic PCI for the discharge in figure 11. The MC layer,  $^3\text{He}$  and D resonance layer are also plotted.  $R_{\text{axis}} = 0.682 \text{ m}$ .

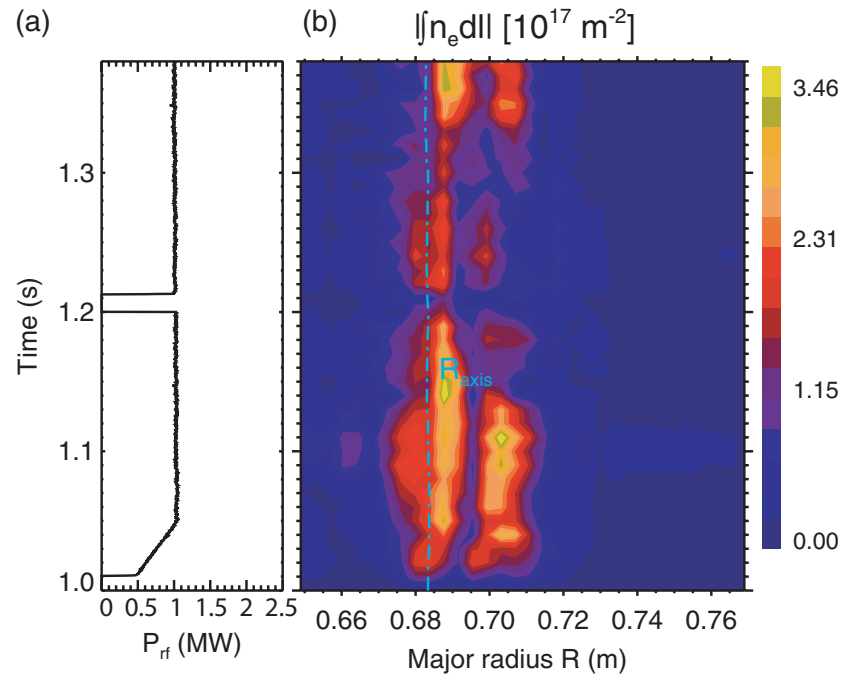


**Figure 15.** A discharge with near-axis mode conversion.  $f_{\text{RF}} = 50 \text{ MHz}$ ,  $B_{\text{axis}} = 5.41 \text{ T}$ ,  $n_{\text{H}}/n_{\text{D}} = 4\%$ ,  $n_{^3\text{He}}/n_{\text{e}} = 11\text{--}12\%$ . (a) RF power versus time, (b) the PCI measured line-integrated fluctuation level versus time and major radius.

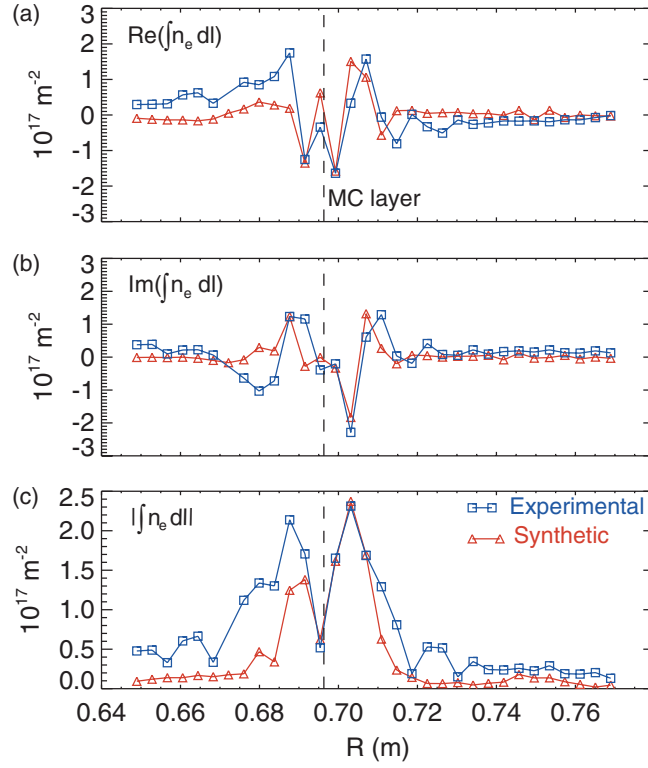


**Figure 16.** Experimental and synthetic PCI line integrated density fluctuations amplitude versus major radius for the discharge in figure 15. (a) Real part, (b) imaginary part, (c) magnitude.

The double hump structure is the result of up-down asymmetry in wavelength of the MC ICWs above and below the mid-plane. In figure 17, the contours of the two-dimensional density fluctuation from TORIC simulation of  $n_\phi = 6$  is plotted. The vertical dashed line in figure 17(b) indicates a PCI chord. It is clearly shown that the ICWs above the mid-plane and below the mid-plane are cancelled out along this chord, whereas the cancellation is smaller in other locations. The wavelengths of the MC ICW above and below the mid-plane are different, which can be estimated from equation (8). For two locations with the same vertical  $|Z|$  above and below the mid-plane,  $k_\perp \sim m/r$  should differ approximately,

$$|\Delta k_\perp| \approx 2 \frac{n_\phi}{R} \frac{B_\phi}{B_{\text{pol}}}, \quad (9)$$

to have a similar  $|k_\parallel|$  to meet the local dispersion equation. To show in more detail, in figure 18 we plot  $B_{\text{pol}}$  contours from EFIT with the density fluctuations from figure 17. Two up-down pairs of ICW are selected and approximate wavelengths,  $\lambda \simeq \lambda_\perp$ , are calculated. The differences in  $k_\perp$  are also labelled in the figure. Using  $n_\phi = 6$  and  $B_{\text{axis}} = 5.41$  T, equation (9) gives  $|\Delta k_{\perp 1}| \simeq 3.1 \text{ cm}^{-1}$  and  $|\Delta k_{\perp 2}| \simeq 3.6 \text{ cm}^{-1}$ , respectively. These values are in good agreement with  $|\Delta k_{\perp 1}| \simeq 3.5 \text{ cm}^{-1}$  and  $|\Delta k_{\perp 2}| \simeq 3.8 \text{ cm}^{-1}$  shown in the figure. This agreement suggests that the double hump structure results from the interference pattern between the MC ICWs above and below the mid-plane. At a smaller  $B_{\text{pol}}$  (near the axis), this pattern is more prominent because the up-down asymmetry in wave number is stronger according to equation (9). Such asymmetry in wavelength is smaller when the MC layer is

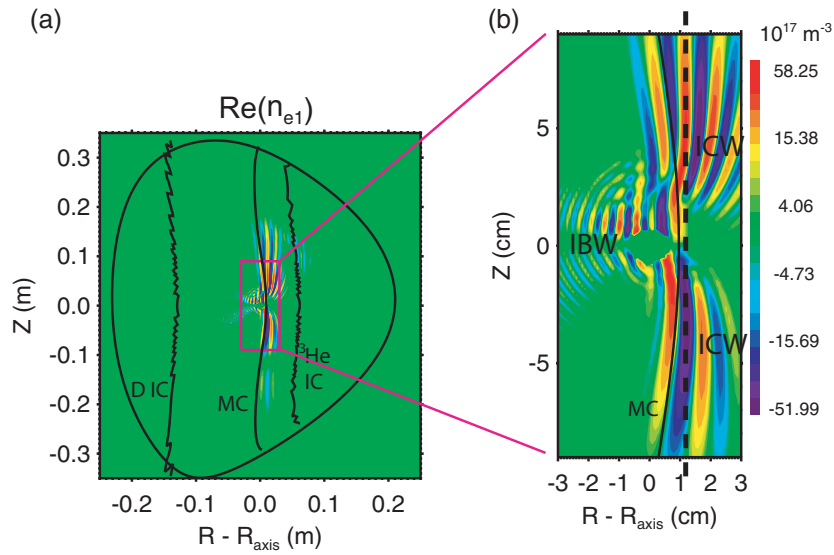


**Figure 17.** Two-dimensional density fluctuations calculated by the synthetic PCI ( $n_\phi = 6$ ). The vertical dashed line in (b) indicates a PCI chord.

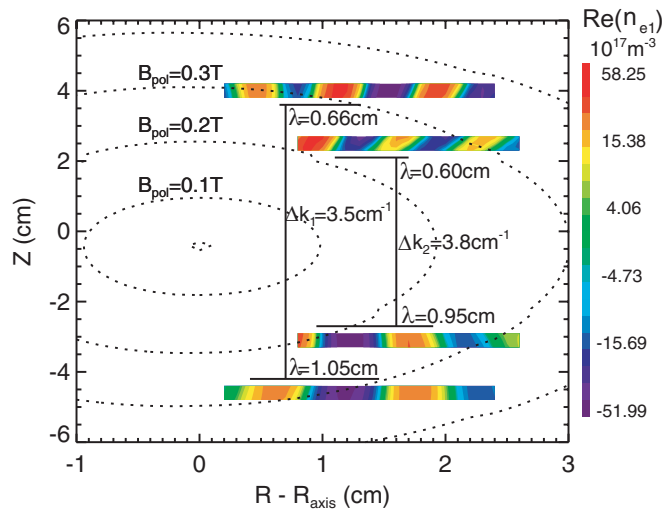


**Figure 18.** MC ICW up-down asymmetry and  $B_{\text{pol}}$ . Dot lines are  $B_{\text{pol}}$  contours, while colour contours are density fluctuations.

off axis (cf figure 7). Equation (9) is not applicable for cases like that in figure 14, where ICWs are at different  $|Z|$ .

In figure 19 we compare the  $k_R$  spectrum of the PCI measurements and the synthetic PCI output. There are three peaks in both spectra. The one near  $k \simeq \pm 0.5 \text{ cm}^{-1}$  is the FW, which is in agreement with the expected FW wave number (cf figure 10(b)). The peak at  $k_R \simeq -0.5 \text{ cm}^{-1}$  is larger than the one at  $k_R \simeq +0.5 \text{ cm}^{-1}$ , suggesting that the inward propagating FW has a larger amplitude than the outward propagating FW. This observation indicates that the FW field in the plasma does not appear as a standard standing-wave pattern.

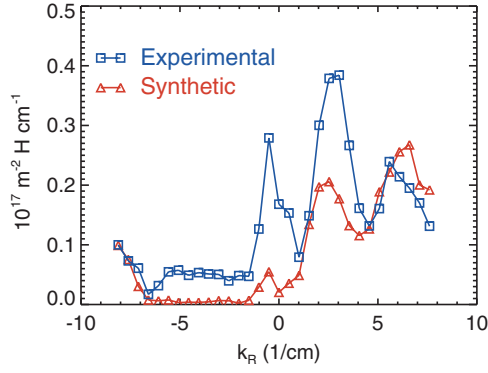


**Figure 19.**  $k_R$  spectra of the experimental and synthetic PCI line integrated density fluctuations for the discharge in figure 15.

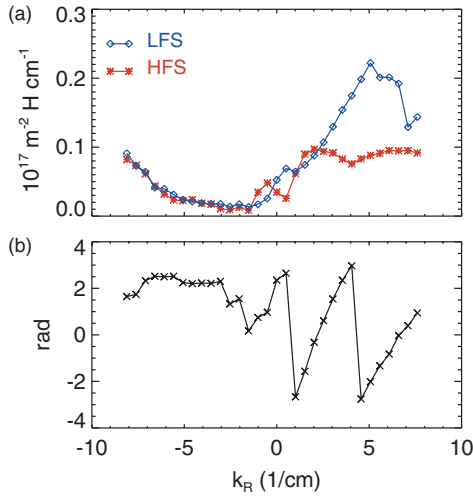


**Figure 20.**  $k_R$  spectra calculated in two separate regions: (a) magnitude, (b) phase difference of the two spectra.

Because of the mode conversion to the MC ICW, the left-cutoff layer  $n_{\parallel}^2 = L$  (e.g. figure 10(b)) no longer acts as a reflection layer for the FWs reflected from the right-cutoff layer  $n_{\parallel}^2 = R$  at the HFS edge. The resulting FW pattern is more like a wave with a load in one end. There are two other broad peaks in figure 19 at  $k \sim 3 \text{ cm}^{-1}$  and  $k \sim 8 \text{ cm}^{-1}$ . Both are definitely from the MC waves. However, more detailed analysis finds that neither peak is solely from the MC IBW nor solely from the MC ICW. In figure 20, we show the result of Fourier transformations of the synthetic PCI output done separately on channels at  $R < 0.69 \text{ m}$  and channels at  $R > 0.69 \text{ m}$  (zeroing-out the remaining channels). Note that the spectrum for all 32 channels is the linear combination of these two complex spectra. The spectra in figure 20(a) are broad, comparable to those in figures 9 and 13. The phase difference of these two complex spectra, shown in figure 20(b), approaches  $\pi$  at  $k_R \sim 4 \text{ cm}^{-1}$ . The destructive combination of these two spectra at  $k_R \sim 4 \text{ cm}^{-1}$  can explain the double peak structure in the  $k_R$  spectra shown in figure 19. The ambiguity in interpreting the simple  $k_R$  spectrum of figure 19 is caused by the fact that multiple waves with similar  $k_R$  exist in a narrow MC region.

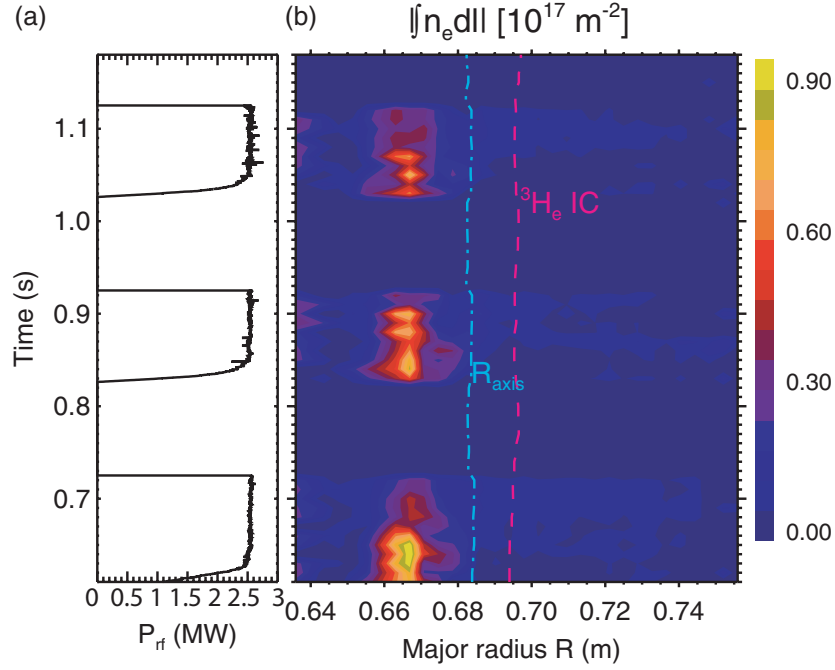


**Figure 21.** A discharge with on-axis mode conversion.  $f_{RF} = 78$  MHz,  $B_{axis} = 7.73$  T,  $n_H/n_D = 5\%$ ,  $n_{^3\text{He}}/n_e = 5\%$ . (a) RF power versus time, (b) the PCI measured line-integrated fluctuation level versus time and major radius.

The near-axis mode conversion at  $\sim 8$  T is different than the one at  $\sim 5.4$  T. In these discharges, the MC IBW is found to be the only MC wave. In figure 21, we show the PCI data of such a discharge at  $B_{axis} = 7.73$  T and  $f_{RF} = 78$  MHz. The MC signals appear at around  $R = 0.66$ – $0.67$  m. Other plasma parameters are  $I_p = 1.2$  MA,  $n_{e0} = 2.1 \times 10^{20} \text{ m}^{-3}$ ,  $T_{e0} = 4.1$  keV and  $T_i \simeq T_e$ ,  $n_H/n_D = 5\%$ .  $R_{axis} = 0.682$  m.  $^3\text{He}$  gas was puffed only for 50 ms in the discharge. The  $^3\text{He}$  concentration is estimated to be  $n_{^3\text{He}}/n_e = 5\%$  by comparing to the TORIC simulations.

For this discharge, the MC IBW is the only MC wave as seen in figure 22, in which the density fluctuations is plotted from the TORIC simulation of  $n_\phi = 7$ . Since  $B_{pol}/B_{tot} \ll 1$ , mode conversion to IBW dominates. In figure 23, the experimental PCI data is compared with the synthetic PCI data versus major radius. The short wavelength wave structure is mostly on the HFS of the MC layer (note the MC layer indicated in the figure is from cold plasma approximation). The detectors in the PCI system are sensitive to wave numbers up to  $k_{lim} \simeq 17 \text{ cm}^{-1}$ , larger than the maximum  $k_R$  determined by the channel separation,  $k_{max} \simeq 8 \text{ cm}^{-1}$ . As a result, waves having  $k_{max} \leq k_R \leq k_{lim}$  may be also detected by the PCI, but appear in the PCI spectrum at  $k_R - 2k_{max}$  owing to the spatial aliasing. In figures 24(a) and (b), we plot the  $k_R$  spectra from both experimental PCI and synthetic PCI. There is a broad peak at  $k_R < -3 \text{ cm}^{-1}$  in figure 24(a). To check whether this part of the spectrum is aliased, we double the total channel number and reduce the separation between channels by half in the synthetic PCI and calculate the  $k_R$  spectrum again. The broad peak at  $k_R < -3 \text{ cm}^{-1}$  in the synthetic PCI spectrum indeed disappears. Instead, the peak at positive  $k_R$  is extended to  $k_R \sim 13 \text{ cm}^{-1}$  as shown in figures 24(b). This result demonstrates that 32 channel PCI does not have adequate spatial resolution for the MC IBW, resulting in spatial aliasing in

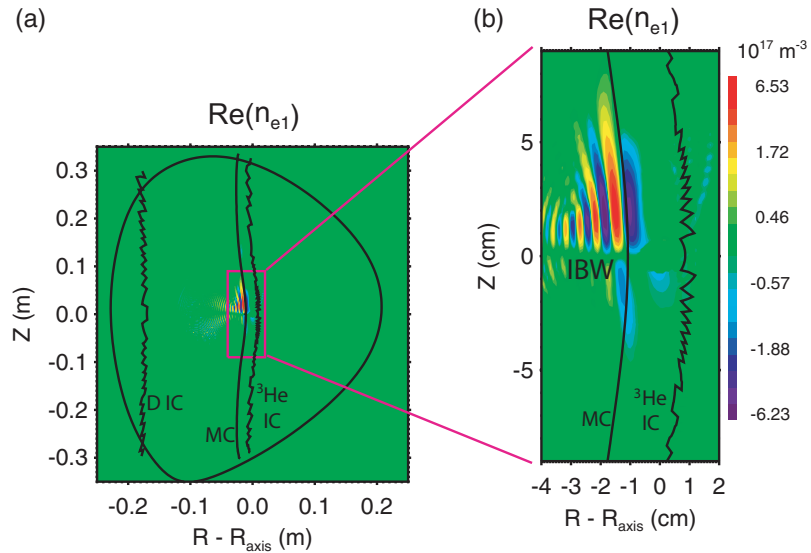


**Figure 22.** Density fluctuations in two-dimensional calculated by the synthetic PCI for the discharge in figure 21 ( $t = 0.64$  s).

the  $k_R$  spectrum. Assuming the part at  $k_R < -3 \text{ cm}^{-1}$  of the experimental PCI spectrum is all aliased and shifting it by  $2k_{\text{max}}$ , we also find a broad MC IBW peak from  $k_R = 2$  to  $13 \text{ cm}^{-1}$  as shown in figure 24(b), in good agreement with the one from the 64 channel synthetic PCI. There are also FW peaks at  $k_R \simeq \pm 0.5 \text{ cm}^{-1}$  in this figure. In figure 25, we plot the dispersion curves for the IBW and FW. The dispersion curve of the MC IBW shows that it has the same range of wave numbers as in figure 24(b). No MC ICW root exists along the magnetic surface tangential to the MC layer. This is the first definitive observation of IBW-only mode conversion by PCI in Alcator C-Mod.

In summary, PCI observations of the near-axis mode conversion at 50 MHz show both the MC IBW and MC ICW. The FW has also been observed in some discharges. The up-down asymmetry of the MC ICW, which is more prominent in near-axis mode conversion than off axis, creates a double hump interference structure, seen in both experiments and simulations. In 8 T near-axis mode conversion, the MC IBW is shown to be the only MC wave because of a small  $B_{\text{pol}}/B_{\text{tot}}$ . The experimental  $k_R$  spectrum of the MC IBW agrees with the synthetic PCI and dispersion curve after spatial aliasing is considered.

#### 4. Discussion and future work

The experimental PCI and synthetic PCI agree very well after multiplying by the correction factors as mentioned in section 2.2. We hypothesize that the absolute calibration of the heterodyne scheme of PCI is the likely explanation. And the calibration needs to be improved. The MC IBW spectrum in 78 MHz near-axis MC discharges has a problem of spatial aliasing. By reducing the separation between the channels, we may be able to obtain the MC IBW spectrum without aliasing ambiguity. The up-down asymmetry of the MC ICW can explain the double hump structure seen in the PCI measurement in 50 MHz near-axis mode conversion and is also clearly shown in the TORIC simulation. However, because of the line integration nature of the present PCI diagnostic, the up-down asymmetry was not measured directly.

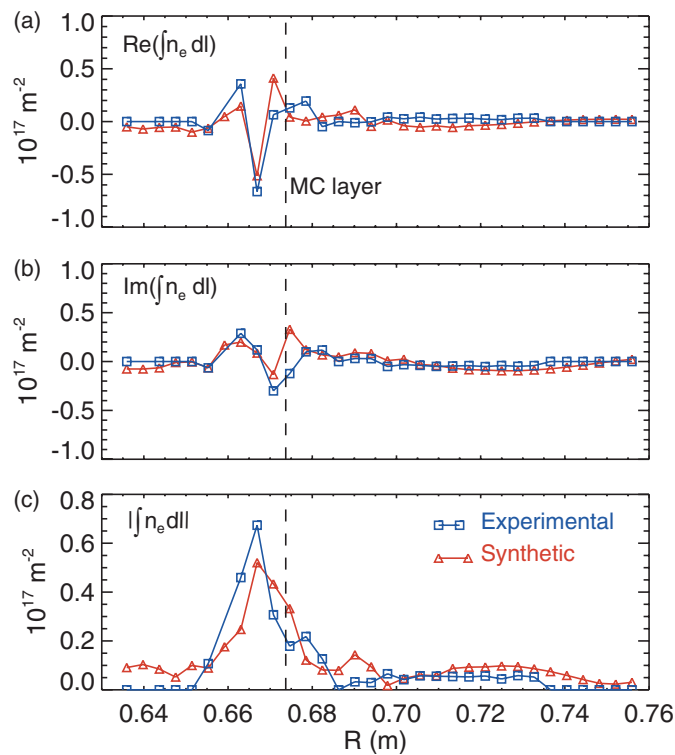


**Figure 23.** Experimental and synthetic PCI line integrated density fluctuations amplitude versus major radius for the discharge in figure 21. (a) Real part, (b) imaginary part, (c) magnitude.

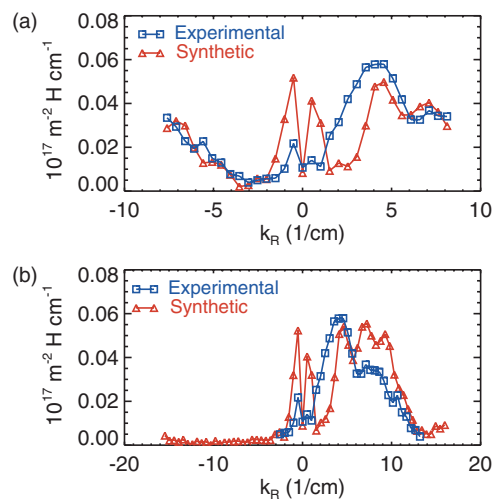


**Figure 24.**  $k_R$  spectra of the experimental and synthetic PCI line integrated density fluctuations for the discharge in figure 21. (a) Usual spectra, (b) all  $k_R < 3 \text{ cm}^{-1}$  in the experimental PCI spectrum are shifted by  $16 \text{ cm}^{-1}$ , whereas the synthetic PCI has twice the number of channels of the experimental PCI.

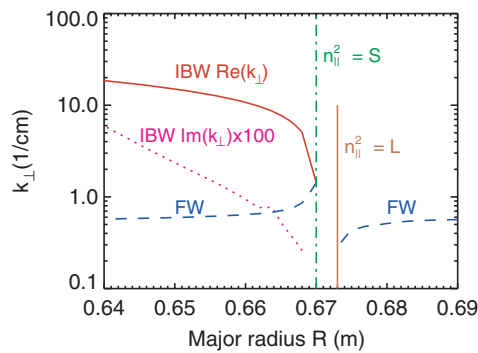


**Figure 25.** Dispersion curves of IBW and FW calculated at the mid-plane. Both the imaginary and real parts of the MC IBW are shown.

In the future, the PCI system will be upgraded to have the capability of vertical spatial localization [29]. After this upgrade, we may be able to experimentally study the mode conversion region in two dimension and new physics can be explored. For example, the low single pass absorption ( $\leq 10\%$ ) by the minority ions of the FW in these plasmas should have generated a strong standing-wave pattern of the FW. We can use the upgraded PCI to measure the phase and strength of the FW near the MC layer, which may influence the MC efficiency and the structure of the MC waves, and study the MC physics in a more detailed fashion.

## 5. Summary

ICRF waves on multiple spatial scales in the mode conversion region of  $D(^3\text{He})$  plasmas have been observed using PCI in the Alcator C-Mod tokamak. Good agreement has been obtained between the experimental observation and the result of a synthetic PCI based upon TORIC. The observed waves include the FW, MC ICW and MC IBW. When the mode conversion layer is off axis, both MC IBW and MC ICW were observed. In the near-axis mode conversion discharges at  $B \sim 5.4\text{ T}$  ( $f_{\text{RF}} = 50\text{ MHz}$ ), a double hump structure was observed experimentally and reproduced by the synthetic PCI. Such structure is an indication of the up-down asymmetry of the MC ICW. The MC IBW has been shown to be the only MC wave in the near-axis mode conversion discharges at  $B \sim 8\text{ T}$  ( $f_{\text{RF}} = 78\text{ MHz}$ ). This work is the first comprehensive experimental and numerical study of ICRF wave phenomena in the mode conversion region of Alcator C-Mod.

## Acknowledgments

The authors thank RF engineer Mr C Schwartz, who died in a plane crash in October 2004, for his substantial contribution to the ICRF system operation. Many thanks also go to Dr E Nelson-Melby and Mr K Jordy in the development of the synthetic PCI. This research used the MIT Plasma Science and Fusion Center Theory Group parallel computational cluster. This work is supported at MIT by US DoE Cooperative Agreement No DE-FC02-99ER54512.

## References

- [1] Porkolab M 1994 Plasma heating by fast magnetosonic waves in tokamaks N Fisch, ed *Advances in Plasma Physics* vol 314 *AIP Conf. Proc.* p 99 (New York: American Institute of Physics)

- [2] Perkins F W 1977 Heating tokamaks via the ion–cyclotron and ion–ion hybrid resonances *Nucl. Fusion* **17** 1197
- [3] Nelson-Melby E, Porkolab M, Bonoli P T, Lin Y, Mazurenko A and Wukitch S J 2003 Experimental observations of mode-converted ion cyclotron waves in a tokamak plasma by phase contrast imaging *Phys. Rev. Lett.* **90** 155004
- [4] Jaeger E F *et al* 2003 Sheared poloidal flow driven by mode conversion in tokamak plasmas *Phys. Rev. Lett.* **90** 195001
- [5] Lin Y *et al* 2004 Investigation of ion cyclotron range of frequencies mode conversion at the ion–ion hybrid layer in Alcator C-Mod *Phys. Plasmas* **11** 2466
- [6] Wright J C, Bonoli P T, Brambilla M, Meo F, D’Azevedo E, Batchellor D B, Jaeger E F, Berry L A, Phillips C K and Pletzer A 2004 Full wave simulations of fast wave mode conversion and lower hybrid wave propagation in tokamaks *Phys. Plasmas* **11** 2473
- [7] Lin Y *et al* 2003 Ion cyclotron range of frequencies mode conversion electron heating in deuterium–hydrogen plasmas in the Alcator C-Mod tokamak *Plasma Phys. Control. Fusion* **45** 1013
- [8] Mantsinen M J *et al* 2004 Localized bulk electron heating with ICRF mode conversion in the JET tokamak *Nucl. Fusion* **44** 33
- [9] Saoutic B, Bécoulet A, Hutter T, Ram A K and Bers A 1996 Mode conversion heating experiments on the Tore Supra tokamak *Phys. Rev. Lett.* **76** 1647
- [10] Bonoli P T *et al* 2000 Mode conversion electron heating in Alcator C-Mod: theory and experiment *Phys. Plasmas* **7** 1886
- [11] Bonoli P T *et al* 1997 Electron heating via mode converted ion Bernstein waves in the Alcator C-Mod tokamak *Phys. Plasmas* **4** 1774
- [12] Majeski R *et al* 1996 Ion cyclotron range of frequency experiments in the tokamak fusion test reactor with fast waves and mode converted ion Bernstein waves *Phys. Rev. Lett.* **5** 764
- [13] Wukitch S *et al* 2005 Ion cyclotron range of frequency mode conversion physics in Alcator C-Mod: experimental measurements and modeling *Phys. Plasmas* **12** 056104
- [14] Phillips C K *et al* 2000 ICRF heating and profile control techniques in TFTR *Nucl. Fusion* **40** 461
- [15] Stix T H 1992 *Waves in Plasmas* (New York: American Institute of Physics)
- [16] Brambilla M 1998 Electron Landau damping of ion Bernstein waves in tokamak plasmas *Nucl. Fusion* **38** 1805
- [17] Brambilla M 1999 Numerical simulation of ion cyclotron waves in tokamak plasmas *Plasma Phys. Control. Fusion* **41** 1
- [18] Porkolab M, Bonoli P T, Lin L, Lin Y, Nelson-Melby E, Parisot A, Rice J E, Schilling G, Wright J C and Wukitch S J 2004 Mode conversion, current drive and flow drive with high power ICRF waves in Alcator C-Mod: experimental measurements and modeling *Proc. 20th IAEA Fusion Energy Conf. (Vilamoura, Portugal)* pp EX/P4–32
- [19] Hutchinson I H *et al* 1994 First results from Alcator-C-Mod *Phys. Plasmas* **1** 1511
- [20] Wukitch S J *et al* 2004 Investigation of performance limiting phenomena in a variable phase ICRF antenna in Alcator C-Mod *Plasma Phys. Control. Fusion* **46** 1479
- [21] Tutt T E 1999  $H_{\alpha}/D_{\alpha}$  spectroscopy on Alcator C-Mod *Master’s Thesis* Massachusetts Institute of Technology
- [22] Heard J W, Watts C, Gandy R F and Phillips P E 1999 High resolution electron cyclotron emission temperature profile and fluctuation diagnostic for Alcator C-Mod *Rev. Sci. Instrum.* **70** 1011
- [23] Mazurenko A 2001 Phase contrast imaging on the Alcator C-Mod tokamak *PhD Thesis* Massachusetts Institute of Technology
- [24] Weisen H 1988 The phase contrast method as an imaging diagnostic for plasma density fluctuations (invited) *Rev. Sci. Instrum.* **59** 1544
- [25] Coda S and Porkolab M 1995 Edge fluctuation measurements by phase contrast imaging on DIII-D *Rev. Sci. Instrum.* **66** 454
- [26] Lao L *et al* 1985 Reconstruction of current profile parameters and plasma shapes in tokamaks *Nucl. Fusion* **25** 1611
- [27] Smithe D N, Phillips C K, Hosea J C, Majeski R P and Wilson J R 1997 Investigation of RF absorption by fast ions and high temperature plasmas using the METS95 wave analysis tool *12th Topical Conf. on Radio Frequency Power in Plasmas* vol 403 *AIP Conf. Proc.* p 367 (New York: American Institute of Physics)
- [28] Nelson-Melby E 2001 Observations and theory of mode-converted ion Bernstein waves in the Alcator C-Mod tokamak *PhD Thesis* Massachusetts Institute of Technology
- [29] Lin L *et al* 2004 Search for TEM and ETG modes with the upgraded PCI diagnostic in Alcator C-Mod *Bull. Am. Phys. Soc.* **49** 73